Biosensors and Bioelectronics 221 (2023) 114925

Contents lists available at ScienceDirect

Biosensors and Bioelectronics

journal homepage: www.elsevier.com/locate/bios

Europium-based metal-organic framework with acid-base buffer structure as electrochemiluminescence luminophore for hyperstatic trenbolone trace monitoring under wide pH range

Lu Zhao, Xianzhen Song, Yuyang Li, Hongying Jia, Nuo Zhang, Qin Wei, Dan Wu *, Huangxian Ju

Collaborative Innovation Centre for Green Chemical Manufacturing and Accurate Detection, School of Chemistry and Chemical Engineering, University of Jinan, Jinan, 250022, Shandong, China

ARTICLE INFO

Keywords:
Eu-MOF
Acid-base buffer structure
Trenbolone trace detection
Wide pH range
Electrochemiluminescence biosensor

ABSTRACT

The wide and even whole pH range electrochemiluminescence (ECL) is attractive for steroid estrogens detection under harsh conditions (such as strong acid and alkali). Herein, we presented an efficient europium-based metal-organic framework (Eu-MOF) as ECL luminophore, which has been synthesized via the specific 2, 4-bis(3, 5-dicarboxyphenylamino)-6-oltriazine (H_4BDPO) ligand with acid-base buffering effect. The functional groups with weak acid and base endowed the H_4BDPO with eight ionogenic group states, thereout different total charges of H_4BDPO were derived, thus high and steady ECL signals of Eu-MOF were acquired under different environments with pH = 1.0–14.0. Most notably, combined with the means of UV–vis, fluorescence spectra, cyclic voltammetry (CV) and density functional theory (DFT) calculations, the Eu-MOF has been explored different luminescence mechanisms with variational total charges. The constructed ECL biosensor based on the Eu-MOF realized sensitive detection of trenbolone under wide pH range (In order to maintain the biological activity of antigen and antibody, the studied pH value is 5–8.5), in which the limits of detection were 3.95 fg/mL (pH = 5.0), 2.36 fg/mL (pH = 7.4) and 5.48 fg/mL (pH = 8.5) respectively. This work provides a considerable method to realize efficient trace detection of steroid estrogens under the wide or even whole pH conditions.

1. Introduction

Steroid estrogens sensitive monitoring under harsh conditions (strong acid or base condition) is a problem demanding prompt solution. Among the reported detection methods, electrochemiluminescence (ECL) can be finely tuned to extensive application fields by simple operation, low background, high sensitivity and stability, such as clinical diagnosis, drug screening, food and environment detection (Song et al., 2018, 2020, 2021; Zhao et al., 2021, 2022; Zhao et al., 2021a,b). Despite great progress in the fabrication of ECL luminophore, it is still highly challenging to prepare high-efficiency luminescent materials with outstanding stability such as good endurance of wide pH range. Until now, graphene quantum dots (GQDs) are found to be stable in only neutral or weak acidic solution, while strong acidic or alkaline conditions always result in reduced fluorescence intensity (Yuan et al., 2015). Gold nanoclusters (AuNCs) show a tendency of fluorescence in the pH range of 5–9, rather than a continuous high signal (Bai et al., 2018). Hence it is crucial to design ECL luminophore with acid-base resistance properties, which can make the constructed ECL devices to work under harsh conditions (strong acid or base condition) and to have high efficiency under dynamic pH range.

Inspired by the self-assembly characteristic of metal-organic frameworks (MOFs) (Kuang et al., 2018; Zhao et al., 2019; Katayama et al., 2019), coassembling the luminophore and acid-base resistance properties components into the same framework as ECL luminophore is a feasible method to realize powerful and robust ECL under wide even whole pH range. Especially in lanthanide-based metal-organic frameworks (Ln-MOFs), lanthanide ions are promising candidates for luminous component owing to their high luminescent quantum yield, narrow and intense band emission, large Stokes shift, long luminescent lifetime, and undisturbed emission wavelength. Moreover, the antenna effect between ligand and lanthanide ions makes Ln-MOFs stronger luminescence (Zhao et al., 2021a,b; Gao et al., 2018; Eliseeva and Buenzli, 2010; Zhang et al., 2018). For this target, an unusual rigid 2, 4-bis(3,

* Corresponding author.
E-mail address: wudan791108@163.com (D. Wu).

https://doi.org/10.1016/j.bios.2022.114925
Received 4 July 2022; Received in revised form 20 October 2022; Accepted 16 November 2022
Available online 24 November 2022

5-dicarboxyphenylamino)-6-oltriazine (H_4BDPO) ligand is noticed for the unique consideration. The H_4BDPO ligand, as a buffer guard in MOF, possesses functional groups with weak acid and base simultaneously (the phenol group is weak acid, the amino and triazine groups are weak bases) to prevent erosion from acidic and alkaline media. This essential characteristic makes Ln-MOFs with H_4BDPO display high ECL performance under wide even whole pH range.

Herein, the assembly of H_4BDPO and Eu^{3+} produced a three-dimensional hyperstable MOF (Eu-BDPO) as luminophore to realize efficient and stable ECL performance under every pH conditions between 1.0 and 14.0. ECL signals and efficiencies showed three different phenomena corresponding to pH environments of 1.0–5.5, 5.5–7.4 and 7.4–14.0 respectively, which resulted from the different total charges of H_4BDPO caused by different assembly modes of eight ionogenic group states under different pH. Three kinds of luminescence mechanisms derived from these were studied by means of UV–vis, fluorescence spectra, cyclic voltammetry (CV) and density functional theory (DFT) calculations. In addition, the constructed ECL biosensor via Eu-BDPO as luminophore can realize sensitive trace detection for trenbolone (TB), which is a new steroid estrogen that affects the human endocrine and reproductive system to trigger testicular cancer or bisexual individuals. The low limit of detections (LOD) of the sensor were 3.95 fg/mL (pH = 5.0), 2.36 fg/mL (pH = 7.4) and 5.48 fg/mL (pH = 8.5) respectively and the broad detection range was 10 fg/mL ~ 100 ng/mL.

2. Experimental section

2.1. Preparation of Eu-BDPO

The materials, regents and apparatus were displayed in the Supporting Information. The preparation process of H_4BDPO was based on a reported reference (He et al., 2018a) and optimized synthetic parameters (Fig. S1). 0.4 mmol of $Eu(NO_3)_3{\cdot}6H_2O$ and 0.2 mmol of H_4BDPO were added in mixture with 16 mL N,N-dimethylformamide (DMF), 2 mL of H_2O and 0.5 mL of HNO_3, the solution was transferred into a Teflon-lined stainless steel autoclave and heated at 120 °C for 24 h. The white crystal was harvested by centrifugation and washed with DMF and H_2O, dried at 60 °C.

2.2. Fabrication of the ECL biosensor

The establishment process of electrode was shown in Fig. 6A. First of all, the thin film of Au was electrodeposited on the polished glassy carbon electrode (GCE) surface by using $HAuCl_4$ (1%) solution. Secondly, 6 μL of TB antibody solution (1 μg/mL) was dropped to connect Au film. Next, 2 μL of BSA, 6 μL of the mixture of different concentrations TB standard substances and antigen@Eu-BDPO (the concentration of antigen was 1 μg/mL) was dropped on electrode in turn. The electrodes were dried at 4 °C after layering process, and then removed the unconnected components via washing with water. In the end, the successfully assembled ECL biosensor was put at 4 °C.

3. Results and discussion

3.1. Characterization of Eu-BDPO

The synthesis process of Eu-BDPO was shown in Fig. 1A. In the X-ray powder diffraction (XRD) patterns (Fig. 1B), the good crystallinity consisted in the as-synthesized Eu-BDPO and obvious peaks identified with the simulated spectrogram (CCDC-1523604) correctly which have showed at 5.68°, 6.80°, 7.66°, 11.16° and 19.87° primarily, ascribed to crystallographic planes of (100), (011), (110), (021) and (320). These bore out the successful preparation of Eu-BDPO. Next, fourier transform infrared (FTIR) measurement was used to characterized functional groups in Eu-BDPO for notarizing its structure. In the FTIR spectrum of H_4BDPO ligand (Fig. 1C), the appearance of phenolic and triazinyl group can be said by the O–H and N–H stretching vibrations at around 3360–3700 cm^{-1}, the wide range absorption peak at 1240–1590 cm^{-1} of the typical breathing vibration of the triazine ring and the C═N group (Song et al., 2021; Kumar et al., 2022; Liang et al., 2017). The characteristic peak of carbonyl asymmetric stretching band (C═O) of –COOH at 1708 cm^{-1} was only found in the H_4BDPO, the new asymmetric

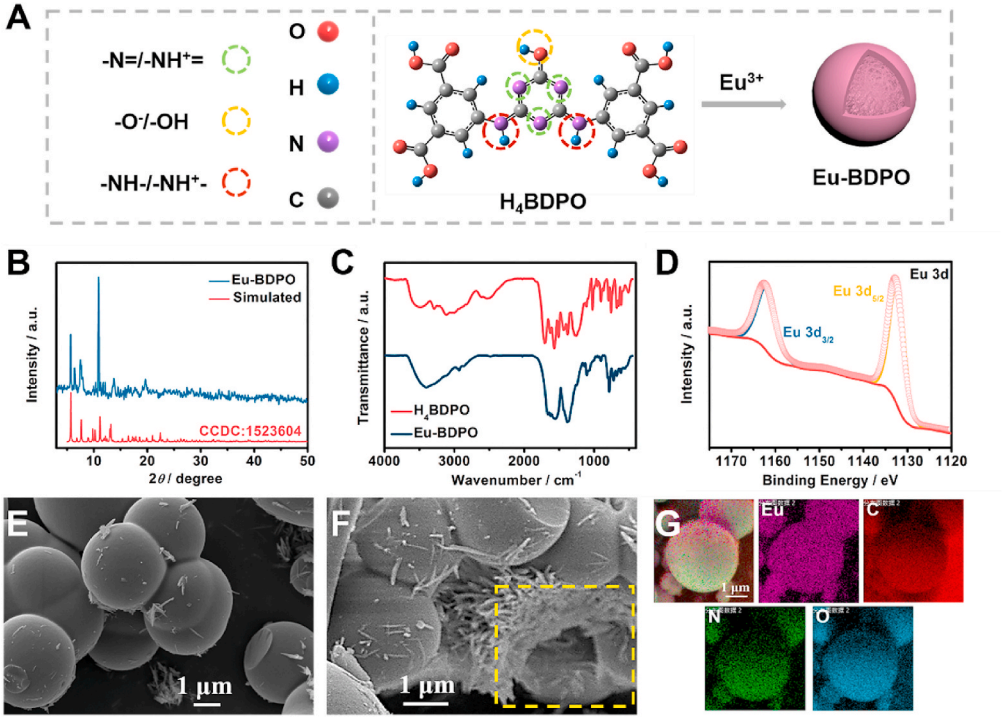

Fig. 1. (A) Synthesis process of Eu-BDPO. (B) XRD pattern of as-synthesized Eu-BDPO and simulated pattern. (C) FT-IR spectra of H_4BDPO ligand and Eu-BDPO. (D) XPS spectrum of Eu 3d in Eu-BDPO. (E–G) SEM images and energy-dispersive X-ray elemental mapping images of Eu-BDPO.

stretching vibration ν_{as} (COO^-) (1610 cm^{-1}) and the symmetric stretching vibration ν_s (COO^-) (1377 cm^{-1}) appeared in the spectrum of Eu-BDPO, implying that the deprotonation of all carboxyl groups in ligand was occurred and they coordinated with Eu^{3+} subsequently (Zhao et al., 2022). The complete chemical composition and valence states of Eu-BDPO were revealed by the X-ray photoelectron spectroscopy (XPS) survey spectrum in Fig. S2A. In detail, the XPS spectrum of Eu 3d was shown in Fig. 1D, in which the binding energies at 1132.4 and 1162.2 eV matched with Eu $3d_{5/2}$ and Eu $3d_{3/2}$ of Eu^{3+}, respectively (Zhao et al., 2021, 2022). For the XPS spectrum of O 1s (Fig. S2B), three obvious binding energy values at 528.9, 530.4 and 531.4 eV were attributable to the O atoms in Eu–O, O^{2-} and C═O. A simple hydrothermal process was conducted of core-shell Eu-BDPO microspheres. Scanning electron microscope (SEM) images (Fig. 1E and F) exhibited the homogeneous microspheres morphology with the diameter of 3.2 μm, and the hollow core-shell structure was discovered from the broken microsphere. The energy-dispersive spectrometry (EDS) results revealed the existence and uniform distribution of Eu, O, C, N elements (Figs. S3 and 1G). With regard to the optical property of Eu-BDPO, the UV–vis–near-infrared (NIR) absorption spectrum of Eu-BDPO (Fig. S4A) revealed its NIR luminescence characteristic in 830–1316 nm region, the particularly striking was the NIR-II characteristic bond from 1000 nm to 1316 nm, which was preferable for detection or treatment of environmental pollution. In contrast, the NIR luminescence characteristic is not available for H_4BDPO ligand (Fig. S4B).

3.2. ECL mechanism and performance of Eu-BDPO

The ECL mechanism was explored by CV and ECL methods. We tested CV and ECL curves of Eu-BDPO in $K_2S_2O_8$ solution and bare phosphate buffer solution (PBS). In Fig. 2A, the reduction peak of Eu-BDPO at −1.20 V was found in both curves (curve a: in $K_2S_2O_8$ solution, curve b: in bare PBS), and no oxidation peak was found, which illustrated that only the electron injected into the lowest unoccupied molecular orbital (LUMO) of Eu-BDPO to form Eu-BDPO$^{\bullet-}$. Combined with the ECL potential-intensity curves (Fig. 2B), the generation of ECL signal was occurred with the aid of $K_2S_2O_8$ coreactant (17441 a.u.), and the weak signal was observed in bare PBS (1000 a.u.), which is similar to that of $K_2S_2O_8$ own. Based on these, the ECL process of Eu-BDPO leaning on $K_2S_2O_8$ was speculated, and the related ECL mechanism was exhibited in Fig. 2C and equation (1) ~ (4) (Zhao et al., 2021a,b):

$$\text{Eu-BDPO} + e^- \rightarrow \text{Eu-BDPO}^{\bullet-} \quad (1)$$

$$S_2O_8^{2-} + e^- \rightarrow SO_4^{2-} + SO_4^{\bullet-} \quad (2)$$

$$\text{Eu-BDPO}^{\bullet-} + SO_4^{\bullet-} \rightarrow \text{Eu-BDPO}^* + SO_4^{2-} \quad (3)$$

$$\text{Eu-BDPO}^* \rightarrow \text{Eu-BDPO} + h\nu \quad (4)$$

The ECL performances of Eu-BDPO were investigated under different pH environments, all ECL tests were used glassy carbon electrodes (GCEs) loaded Eu-BDPO under the optimized conditions (Fig. S5). The ECL curves with same measurement time segment under every pH coreactant solution were spliced together and exhibited in Fig. 2D. The measured ECL signals were 5700 a.u. approximately when the ambient pH was about 1.0 and 2.0. Then an escalating trend motivated the intensity to increase until the signal reached 17,414 a.u. at pH = 5.5, which remained stable in a stage from 5.5 to 7.4. Further, as the pH of the environment increased, the ECL signals gradually decreased. A sharp decrease occurred while pH = 10.0, and finally the signals tended to be stable at pH = 12.0–14.0 with intensity of 7746 a.u.. In addition, the ECL work curves in a period of time under acidic, weak acidic, neutral, and alkaline environments respectively can always maintain good stability (Fig. 2E).

The ECL and CV measurements were utilized to calculate ECL efficiencies of Eu-BDPO by the equation (Zhao et al., 2021a,b; Dennany et al., 2006):

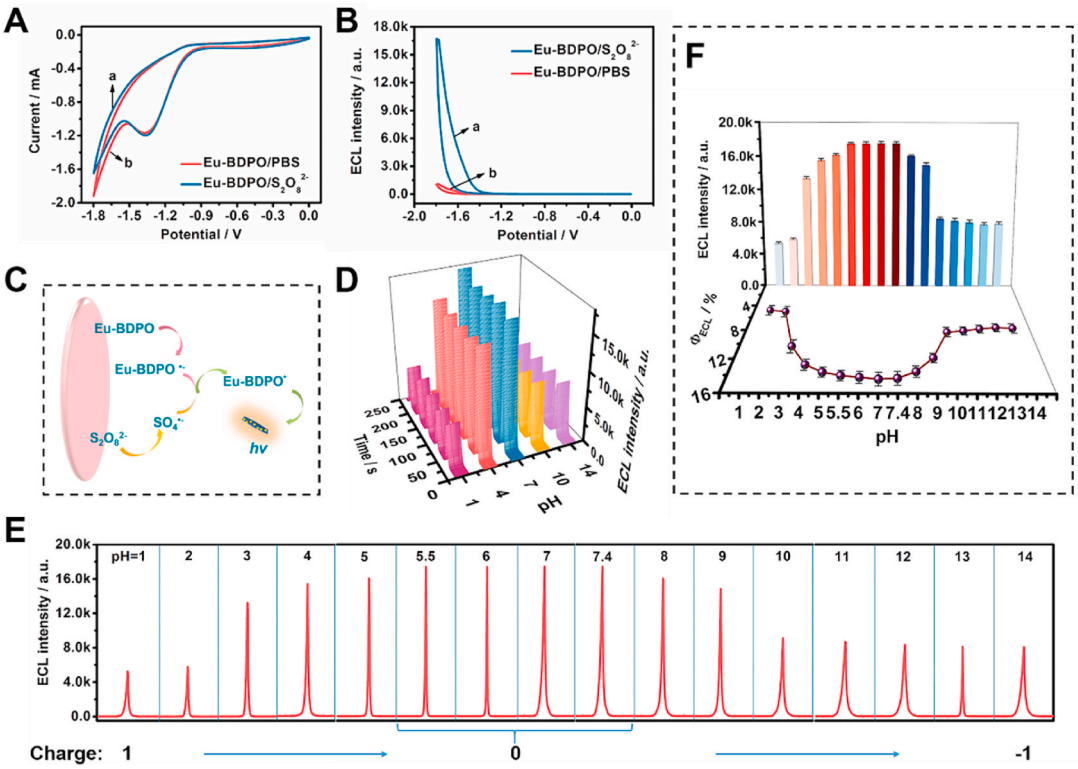

Fig. 2. (A–B) CV and ECL-potential curves of Eu-BDPO in (a) bare PBS and (b) PBS contained $K_2S_2O_8$ (80 mM). (C) The related ECL mechanism of Eu-BDPO in $K_2S_2O_8$. (D) Stability of the ECL signals under the same working times and different pH conditions. (E) ECL signals of electrodes loaded Eu-BDPO under pH from 1.0 to 14.0. (F) ECL signals and efficiencies of electrodes loaded Eu-BDPO under different pH conditions. Error bars = SD, (n = 3).

$\Phi_{ECL} = \Phi^{\circ}_{ECL}(IQ^{\circ}_f/Q_f I^{\circ})$

. In particular, I and I° are the ECL signals in the Eu-BDPO/$K_2S_2O_8$ and reference systems respectively, Q_f and Q°_f are the corresponding faradaic charge went through electrodes, in which the reference system is 1 mM $[Ru(bpy)_3]^{2+}$ in 0.1 M (TBA)BF_4/acetonitrile solution. The Φ°_{ECL} represents the ECL efficiency, that is 5.0%. According to the calculation results, the similar trends were also presented in the ECL efficiencies of Eu-BDPO under pH = 1.0–14.0 (Fig. 2F), which were superior to most $[Ru(bpy)_3]^{2+}$ and $[Ru(bpy)_3]^{2+}$-based luminophors, and the maximum at pH = 5.5–7.4 were about 14.0%. The results described above could draw that Eu-BDPO owns strong acid and alkali resistance, as well as high ECL performance in the whole pH range, especially in the pH of 5.5–7.4.

3.3. Luminescence mechanisms under different pH conditions

According to the references, the -O$^-$/$^-$OH, -NH-/-NH$^+$- and –N = /-NH$^+$ = pairs endow H_4BDPO with buffering effect, which makes the total charge of H_4BDPO change from 1 to −1 in different environments with pH = 1.0–14.0. The generation of total charge in different conditions was depended on the independence or combination of eight ionogenic group states of H_4BDPO. When pH = 1.0, the total charge is 1, and then the total charge decreases until the value is 0 at pH 5.5. From pH = 7.4, the number of negative charges increases until the total charge rises to −1 at pH = 12.0 and remains till pH = 14.0 (He et al., 2018a). Since the change law of total charge in H_4BDPO is similar to that of ECL signal of Eu-BDPO (Figs. S6 and 2F), we explored the luminescence mechanisms of Eu-BDPO under different conditions according to the change principle of total charge reasonably. The luminescence mechanisms were investigated by CV, UV–vis spectra, fluorescence spectra, the DFT calculations by PBEPBE method and 6–31 G* basis set in Gaussian09 program (Alsmail et al., 2014; Li et al., 2017). The lowest unoccupied molecular orbital (LUMO) and highest occupied molecular orbital (HOMO) energy level of Eu^{3+} was calculated by CV and UV–vis measurements (Yan et al., 2021; Yang et al., 2013) (Fig. S7), and that of H_4BDPO was calculated by DFT. The HOMO and LUMO energy levels and the spin isodensity surfaces of H_4BDPO were exhibited. Following the calculation rules, we explored the luminescence mechanism cases where the number of charges was 1, 0 and −1 respectively.

The ligand has positive charge under pH = 1.0–5.5, where the positive charge number is 1 when pH = 1.0. Therefore, CV, UV–vis, fluorescence tests and theoretical calculations were carried out in the pH = 1.0 environment to discuss the luminescence behavior of Eu-BDPO involved by H_4BDPO with positive charge. In Fig. 3A, the UV–vis absorption peaks of Eu^{3+} and Eu-BDPO were 394 and 297 nm (Ahlawat et al., 2018; Lai et al., 2021). The absorption peak localized at 297 nm was assigned to the Eu^{3+}-O^{2-} electron transfer (Lai et al., 2021). The excitation peak of Eu-BDPO was 399 nm, which attributed to the $^7F_0$-$^5L_6$ transition of the Eu^{3+} (Mani et al., 2018). The emission peaks of Eu-BDPO were 533.5, 589 and 803 nm, which originated from the emission of H_4BDPO (Yan et al., 2021; He et al., 2018b), and the primary emission band at 533.5 nm belonged to the HOMO-LUMO+1 electron transition of the H_4BDPO (Fig. 3B and S8A). As can be seen in Fig. 3C, the E_{LUMO} of Eu^{3+} and the E_{LUMO+1} of H_4BDPO were −2.51 and −5.57 eV, the E_{HOMO} of Eu^{3+} and H_4BDPO were −5.62 and −8.52 eV, which fitted with electron transfer from the Eu^{3+} to the ligand-centered π*-type orbitals. These provided reasonable evidences of a luminescence mechanism occurring in the form of metal-to-ligand charge transfer (MLCT) under pH = 1–5.5.

Next, the ligand has no charge at pH = 5.5–7.4. The UV–vis absorption bands of Eu-BDPO (Fig. 4A) at 237 and 276 nm matched the characteristic peaks of Eu^{3+} and H_4BDPO severally. The excitation bands of Eu-BDPO (Fig. 4B) at 271 and 297 nm were assigned to the π-π* transitions of the ligand and the $^7F_6$-^9D transition of Eu^{3+}-O^{2-} (Lai et al.,

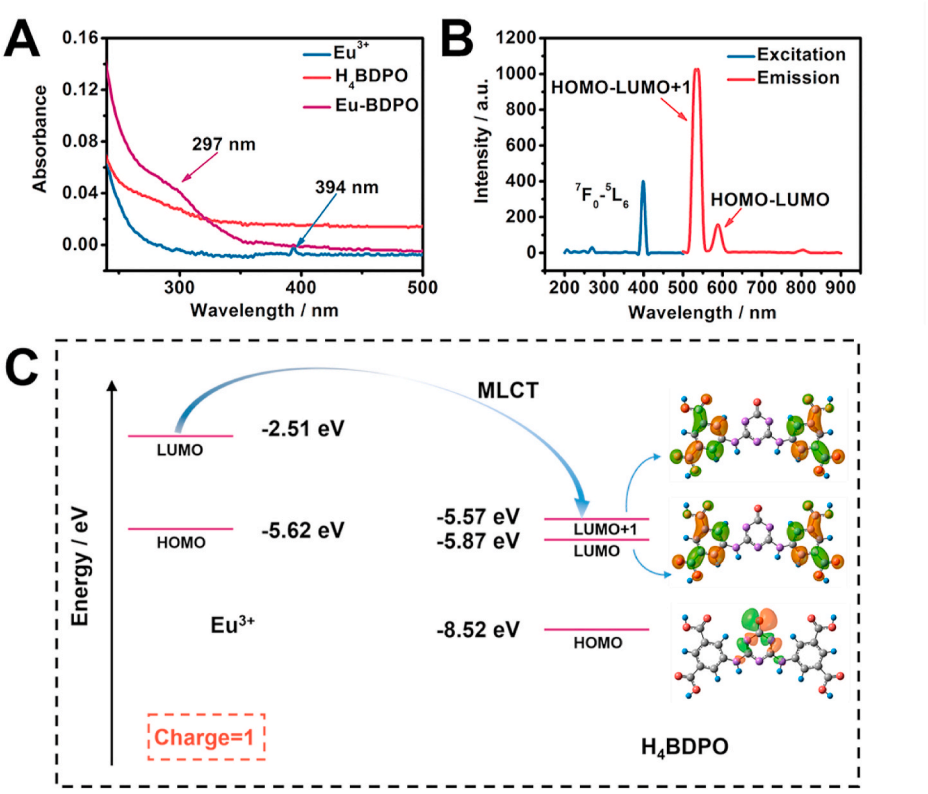

Fig. 3. (A) UV–vis spectra of Eu-BDPO, H_4BDPO and Eu^{3+} under the total charge of ligand was 1. (B) Fluorescence excitation emission spectra of Eu-BDPO under the total charge of ligand was 1. (C) The HOMO, LUMO energy levels of H_4BDPO and Eu^{3+}, the spin isodensity surfaces of H_4BDPO, and the supposed luminescence mechanism of Eu-BDPO under the total charge of ligand was 1.

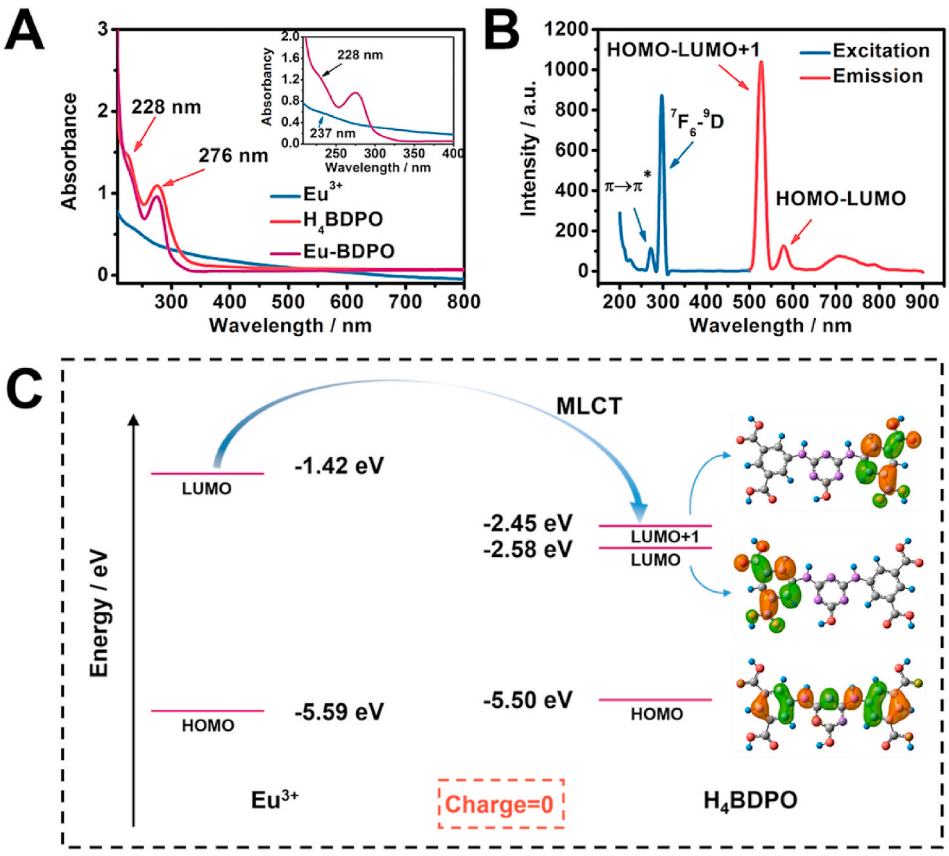

Fig. 4. (A) UV–vis spectra of Eu-BDPO, H_4BDPO and Eu^{3+} under the total charge of ligand was 0. (B) Fluorescence excitation emission spectra of Eu-BDPO under the total charge of ligand was 0. (C) The HOMO, LUMO energy levels of H_4BDPO and Eu^{3+}, the spin isodensity surfaces of H_4BDPO, and the supposed luminescence mechanism of Eu-BDPO under the total charge of ligand was 0.

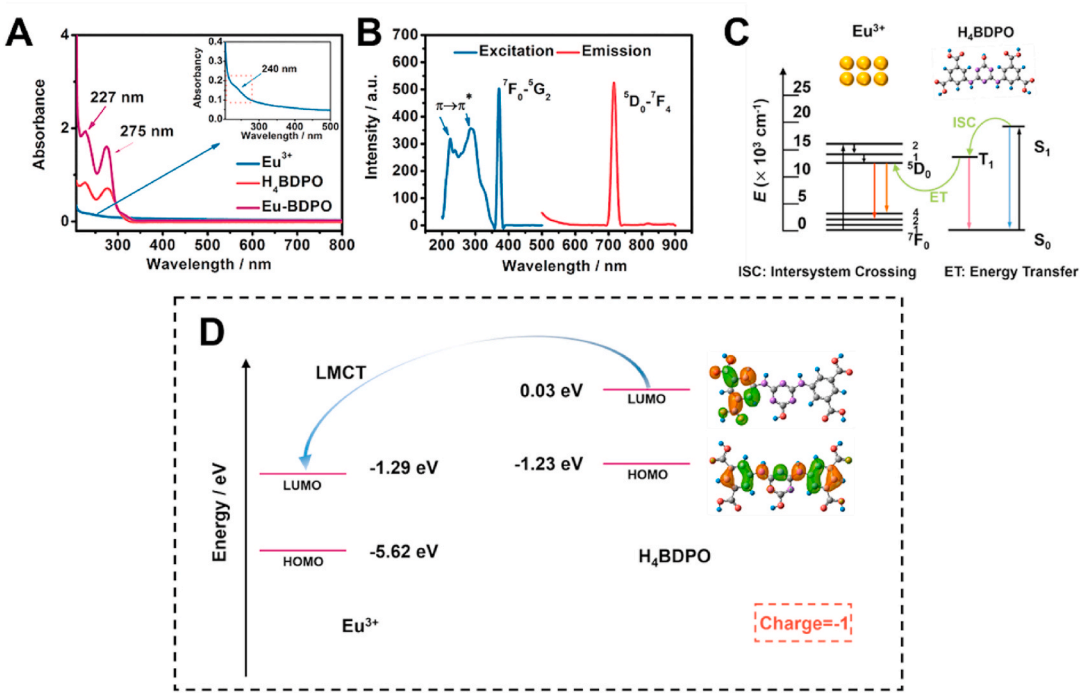

Fig. 5. (A) UV–vis spectra of Eu-BDPO, H_4BDPO and Eu^{3+} under the total charge of ligand was −1. (B) Fluorescence excitation emission spectra of Eu-BDPO under the total charge of ligand was −1. (C) Simple model for energy-transfer process from H_4BDPO to Eu^{3+} and the *f-f* transition luminescence mechanism of Eu^{3+} in Eu-BDPO. (D) The HOMO, LUMO energy levels of H_4BDPO and Eu^{3+}, the spin isodensity surfaces of H_4BDPO, and the supposed luminescence mechanism of Eu-BDPO under the total charge of ligand was −1.

2021), the emission peaks of Eu-BDPO at 533.5, 589 and 803 nm were originated from the emission of H_4BDPO (Fig. S8B). Moreover, the HOMO and LUMO orbitals were calculated in −5.59 and −1.42 eV. Combined with the DFT calculations, the electrons were transmitted from the LUMO orbital of Eu^{3+} to the LUMO+1 and LUMO orbitals of H_4BDPO (E_{LUMO+1} = −2.45 eV, E_{LUMO} = −2.58 eV), the holes were feebly transferred from the HOMO orbital of Eu^{3+} to that of H_4BDPO (E_{HOMO} = −5.50 eV) (Fig. 4C). These provided reasonable evidences of a luminescence mechanism occurring in the form of MLCT under pH = 5.5–7.4.

Finally, the ligand has negative charge under pH = 7.4–14.0, the charge number is -1 when pH = 12.0–14.0. The consistent UV–vis absorption peaks of H_4BDPO and Eu-BDPO distributed in 227 and 275 nm (Fig. 5A), which originated from π-π* transition in the H_4BDPO structure, and revealed that the H_4BDPO center generated electron transport. In the fluorescence spectrum of Eu-BDPO (Fig. 5B), the wide excitation bond from 200 to 360 nm belonged to the π-π* transitions of the ligand (Fig. S8C) (Li et al., 2017; Yang et al., 2013), the narrow and high excitation peak at 370 nm was derived from the $^7F_0$-$^5G_2$ transition of Eu^{3+} (Zhao et al., 2021a,b; Mani et al., 2018). Furthermore, a strong emission narrowband of 717 nm was triggered by the $^5D_0$-$^7F_4$ transition of Eu^{3+} (Zhao et al., 2021a,b; Mani et al., 2018). The UV–vis spectrum and CV curve of Eu^{3+} and DFT calculations of H_4BDPO with the Gaussian 09 program (Fig. 5C) demonstrated that this ligand-to-metal charge transfer (LMCT) was from the LUMO localized on the H_4BDPO (E_{LUMO} = 0.03 eV) to the LUMO localized on Eu^{3+} (E_{LUMO} = −1.29 eV). Persuasively, the DFT calculations were studied the first excited singlet state (S_1) and first excited triplet state (T_1) of H_4BDPO. The simple model of energy-transfer process in antenna effect was depicted via matching with the excited state energy level of Eu^{3+}. As can be seen in Fig. 5D, thanks to the suitable difference between T_1 energy of H_4BDPO and excited state energy of Eu^{3+}, the ligand H_4BDPO was excited to its S_1 with an excitation energy of 19479.10 cm^{-1} firstly. Next the electron was transferred to triplet ground state (T_0) through intersystem crossing (ISC). Then the ligand H_4BDPO sensitized Eu^{3+} via nonradiative energy transmission with a phosphorescent emission energy of 14003.40 cm^{-1}, bearing out the antenna effect-induced energy transfer from H_4BDPO to Eu^{3+}. These provided reasonable evidences of a luminescence mechanism occurring in the form of LMCT under pH = 7.4–14.0.

3.4. Application of ECL biosensor for TB detection

Based on the luminescence mechanism of Eu-BDPO, we constructed a competitive ECL biosensor using Eu-BDPO as ECL luminophore and the standard substance of TB as target to research the high-efficiency trace monitoring of TB in water environment. The assembly process of ECL biosensor was shown in Fig. 6A, and the CV and EIS tests were conducted to attest the successful construction of the biosensor (Fig. S9). For the competitive mechanism of the constructed ECL biosensor, firstly, the antibodies were connected to the Au layer deposited on the electrode surface through Au–S bond. Afterwards, TB standard substance and antigen@Eu-BDPO were modified on assembled electrodes. ECL signals were generated by Eu-BDPO, and the changes of the ECL signals were realized by the competition for specific binding sites of TB antibodies between the TB standard substances and antigens. Specifically, as the concentrations of TB standard samples gradually increased, the binding

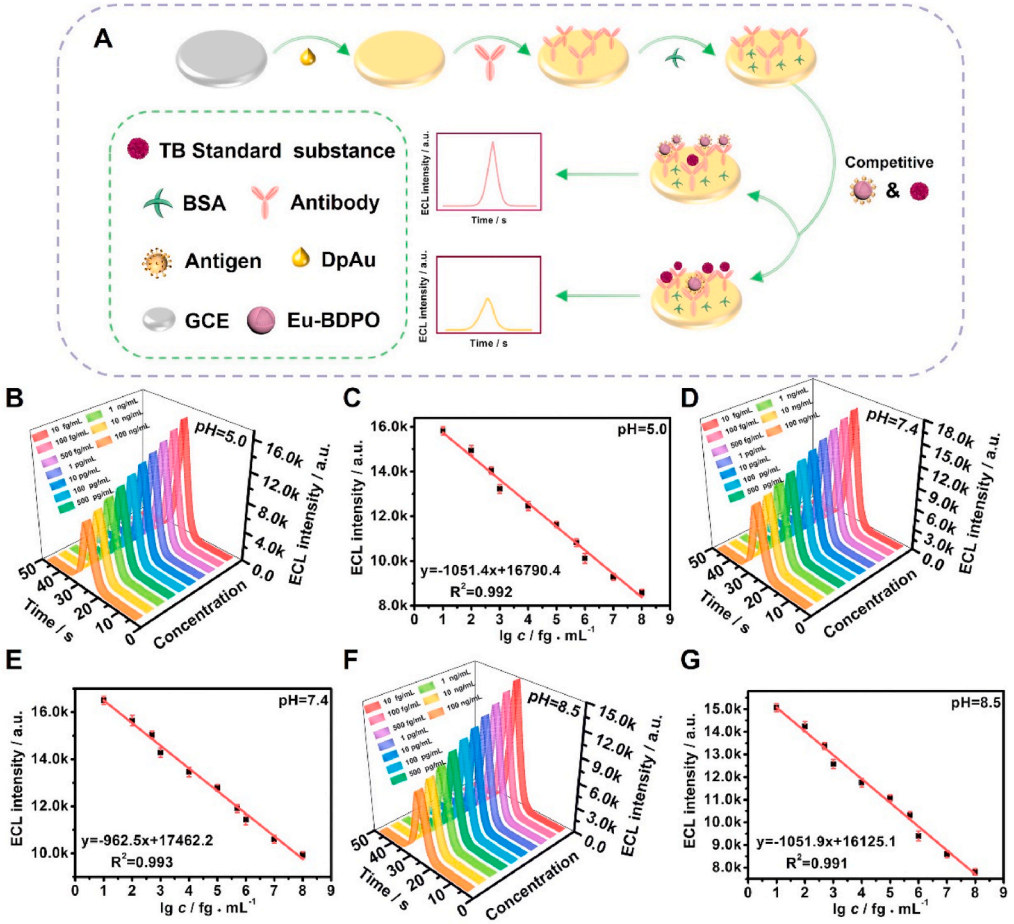

Fig. 6. (A) The fabrication process of the competitive ECL biosensor. ECL intensity-time curves with a wide concentration range of 10 fg/mL~100 ng/mL under different pH conditions (B) 5.0, (D) 7.4 and (F) 8.5. The corresponding linear equation of the TB standard substance concentrations and ECL signals under different pH conditions (C) 5.0, (E) 7.4 and (G) 8.5. Error bars = SD, (n = 3). All experiments were tested under optimal conditions.

amount of antigen@Eu-BDPO gradually decreased, leading to the quenched ECL signals. The quantitative detection for TB was conducted by analyzing the ECL signals that vary with the concentrations of the standard substance of TB under the optimized conditions. Under the premise of not destroying the biological activity of antigen and antibody, the work condition of pH of the ECL biosensors is 5–8.5. Compared to other ECL biosensors that only have the strongest detection capability at an optimal pH condition, the constructed biosensor can achieve high and stable ECL performance at pH range in 5–8.5 (Fig. S10). Further, three pH values (5, 7.4 and 8.5) of three luminescence mechanisms were selected to test ECL performance of the biosensor. As can be seen in Fig. 6B–G, the ECL signals decreased linearly as the TB standard substance concentrations increased (10 fg/mL~100 ng/mL) in the same time period under three pH conditions, the linear equation were $I = -1051.4 \lg c + 16790.4$ ($R^2 = 0.992$, pH = 5.0), $I = -962.5 \lg c + 17462.2$ ($R^2 = 0.993$, pH = 7.4) and $I = -1051.9 \lg c + 16125.1$ ($R^2 = 0.991$, pH = 8.5) respectively, and the calculated LOD were 3.95 fg/mL, 2.36 fg/mL and 5.48 fg/mL respectively, which were lower than the reported detection methods for TB (Table S1). Moreover, the constructed ECL sensor had outstanding reproducibility with the relative standard deviation (RSD) of 3.2% (Fig. S11) and good selectivity under various interferents (100 ng/mL) and mixture (100 ng/mL TB + 100 ng/mL interferents) (Fig. S12). These results revealed the ECL sensor constructing by Eu-BDPO can all realize efficient trace detection of TB in three charge types under pH range of 5–8.5.

Importantly, the real samples analysis of the constructed ECL biosensor was conducted. The initial concentrations of real water samples were obtained from three rivers and measured 3 times to acquire averages. Then the recovery rates and RSD were calculated after the standard addition method, which were 96.7–103% and 1.0–2.7% respectively. From the high recovery rates and low RSD value, the good accuracy and precision of the established ECL biosensor were confirmed. The concerned data were shown in Table S2. To sum up, the assembled ECL biosensor had excellent practicability and met the need of trace detection of environmental estrogen in the real water environment absolutely.

4. Conclusion

An efficient ECL biosensor under wide pH range was constructed by the Eu-MOF (Eu-BDPO) as luminophore with acid-base resistance properties to realize trace detection of TB. The Eu-BDPO was synthesized via the specific H_4BDPO ligand. Because the -O^-/$^-$OH, -NH-/-NH^+- and –N=/-NH^+= pairs vest in weak acid and base pairs, the H_4BDPO has the function of acid-base buffer, which makes the Eu-BDPO ECL operate consistently and vigorously in the full pH range. The different ionogenic group states of H_4BDPO make it has different total charge under different pH conditions. Based on UV–vis, fluorescence spectra, CV and DFT calculations, we certified the different luminous mechanisms of Eu-BDPO, in which the MLCT process occurred when the total charge was 0–1 and the LMCT process occurred when the total charge was -1–0. Combined with ECL results, the energy transfer rate increased as the total charge changes from - 1 to 0. Then, when the total charge changes from 0 to 1, the energy transfer rate decreased, and the energy transfer rate when the total charge is - 1 is greater than that when the total charge is 1. With the change of total charge, ECL signal fluctuated regularly, but it remained at a high level and was very stable. Moreover, Eu-BDPO had been able to construct biosensor that is efficient to detect TB at the maximum operating pH region (5–8.5) with low LOD 3.95 fg/mL (pH = 5.0), 2.36 fg/mL (pH = 7.4) and 5.48 fg/mL (pH = 8.5) respectively. Therefore, this work would provide a method to realize more practical and more sensitive monitoring for steroid estrogens under wide or even full pH conditions.

CRediT authorship contribution statement

Lu Zhao: Conceptualization, Data curation, Writing – original draft. **Xianzhen Song:** Methodology, Data curation, Writing – review & editing. **Yuyang Li:** Methodology. **Hongying Jia:** Formal analysis. **Nuo Zhang:** Methodology, Supervision. **Qin Wei:** Funding acquisition, Formal analysis. **Dan Wu:** Funding acquisition, Project administration, Writing – review & editing. **Huangxian Ju:** Funding acquisition.

Declaration of competing interest

The authors declare that they have no known competing financial interests or personal relationships that could have appeared to influence the work reported in this paper.

Data availability

Data will be made available on request.

Acknowledgments

This work was supported by the Young Taishan Scholars Program of Shandong Province (tsqn201909124), the National Natural Science Foundation of China (22274063), the Project of “20 items of University” of Jinan (2019GXRC018), the Innovation Team Project of Colleges and Universities in Jinan (2019GXRC027). All of authors express their sincere thanks.

Appendix A. Supplementary data

Supplementary data to this article can be found online at https://doi.org/10.1016/j.bios.2022.114925.

References

Alsmail, N.H., Suyetin, M., Yan, Y., Cabot, R., Krap, C.P., Lü, J., Easun, T.L., Bichoutskaia, E., Lewis, W., Blake, A.J., Schrçder, M., 2014. Analysis of high and selective uptake of CO_2 in an oxamide-containing $\{Cu_2(OOCR)_4\}$-Based metal-organic framework. Chem. Eur J. 20, 7317–7324.

Ahlawat, R., Rani, N., Goswami, B., 2018. Synthesis and characterizations of Eu_2O_3 nanocrystallites and its effect on optical investigations of Eu^{3+}, Eu^{2+}: SiO_2 nanopowder. J. Alloys Compd. 743, 126–135.

Bai, X.L., Xu, S.Y., Wang, L.Y., 2018. Full-range pH stable Au-clusters in nanogel for confinement-enhanced emission and improved sulfide sensing in living cells. Anal. Chem. 90, 3270–3275.

Dennany, L., Hogan, C., Keyes, T., Forster, R.J., 2006. Effect of surface immobilization on the electrochemiluminescence of ruthenium-containing metallopolymers. Anal. Chem. 78, 1412–1417.

Eliseeva, S., Buenzli, J.C.G., 2010. Lanthanide luminescence for functional materials and bio-sciences. Chem. Soc. Rev. 1, 189–227.

Gao, Y.X., Yu, G., Liu, K., Wang, B., 2018. Luminescent mixed-crystal Ln-MOF thin film for the recognition and detection of pharmaceuticals. Sensor Actuat B-Chem. 257, 931–937.

He, H.M., Sun, Q., Gao, W.Y., Perman, J.A., Sun, F.X., Zhu, G.S., Aguila, B., Forrest, K., Space, B., Ma, S.Q., 2018a. A stable metal-organic framework featuring a local buffer environment for carbon dioxide fixation. Angew. Chem., Int. Ed. 57, 4657–4662.

He, H.M., Zhu, Q.Q., Sun, F.X., Zhu, G.S., 2018b. Two 3D metal-organic frameworks based on Co^{II} and Zn^{II} clusters for knoevenagel condensation reaction and highly selective luminescence sensing. Cryst. Growth Des. 18, 5573–5581.

Katayama, Y., Kalaj, M., Barcus, K.S., Cohen, S.M., 2019. Self-assembly of metal-organic framework (MOF) nanoparticle monolayers and free-standing multilayers. J. Am. Chem. Soc. 141, 20000–20003.

Kuang, X., Luo, Y.C., Kuang, R., Wang, Z.L., Sun, X., Zhang, Y., Wei, Q., 2018. Metal organic framework nanofibers derived Co_3O_4-doped carbon-nitrogen nanosheet arrays for high efficiency electrocatalytic oxygen evolution. Carbon 137, 433–441.

Kumar, V., Teotia, J., Yadav, A.K., 2022. Vibrational (FT-Raman and FTIR) spectroscopic study, molecular structure, thermodynamic properties and non-linear optical properties of benzyl-3-oxopyperazine-1-carboxylate by density functional theory. Mater. Today Proc. https://doi.org/10.1016/j.matpr.2022.02.185.

Lai, Z.B., Ye, J., Xiong, J., 2021. Energy transfer processes and structure of carboxymethyl cellulose-Tb/Eu nanocomplexes with color-tunable photoluminescence. Carbohydr. Polym. 271, 118386.

Li, X.Y., Shi, W.J., Wang, X.Q., Ma, L.N., Hou, L., Wang, Y.Y., 2017. Luminescence modulation, white light emission, and energy transfer in a family of lanthanide

metal–organic frameworks based on a planar π-conjugated ligand. Cryst. Growth Des. 17, 4217–4224.
Liang, Q.H., Li, Z., Bai, Y., Huang, Z.H., Kang, F.Y., Yang, Q.H., 2017. Reduced-sized monolayer carbon nitride nanosheets for highly improved photoresponse for cell imaging and photocatalysis. Sci China Mater 60 (2), 109–118.
Mani, R., Jiang, H.D., Gupta, S.K., Li, Z.Q., Duan, X.L., 2018. Role of synthesis method on luminescence properties of europium(II, III) ions in β-Ca_2SiO_4: probing local site and structure. Inorg. Chem. 57, 935–950.
Song, X.Z., Li, X.J., Wei, D., Feng, R., Yan, T., Wang, Y.G., Ren, X., Du, B., Ma, H.M., Wei, Q., 2018. CuS as co-reaction accelerator in PTCA-$K_2S_2O_8$ system for enhancing electrochemiluminescence behavior of PTCA and its application in detection of amyloid-β protein. Biosens. Bioelectron. 126, 222–229.
Song, X.Z., Shao, X.R., Dai, L., Fan, D.W., Ren, X., Sun, X., Luo, C.N., Wei, Q., 2020. Triple amplification of 3,4,9,10-perylenetetracarboxylic acid by Co^{2+}-based metal-organic frameworks and silver-cysteine and its potential application for ultrasensitive assay of procalcitonin. ACS Appl. Mater. Interfaces 12, 9098–9106.
Song, X.Z., Zhao, L., Luo, C.N., Ren, X., Yang, L., Wei, Q., 2021. Peptide-based biosensor with a luminescent copper-based metal-organic framework as an electrochemiluminescence emitter for trypsin assay. Anal. Chem. 93, 9704–9710.
Yan, M.X., Feng, S.N., Yu, L.Y., Xue, Y., Huang, J.S., Yang, X.R., 2021. Label-free immunosensor for cardiac troponin I detection based on aggregation-induced electrochemiluminescence of a distyrylarylene derivative. Biosens. Bioelectron. 192, 113532.
Yang, C.L., Xu, J., Ma, J.Y., Zhu, D.Y., Zhang, Y.F., Liang, L.Y., Lu, M.G., 2013. The effect of two additional Eu^{3+} lumophors in two novel trinuclear europium complexes on their photoluminescent properties. Photochem. Photobiol. Sci. 12, 330–338.
Yuan, F.L., Ding, L., Li, Y.C., Li, X.H., Fan, L.Z., Zhou, S.X., Fang, D.C., Yang, S.H., 2015. Multicolor fluorescent graphene quantum dots colorimetrically responsive to all-pH and a wide temperature range. Nanoscale 7, 11727–11733.
Zhang, Q.S., Wang, J., Kirillov, A.M., Dou, W., Xu, C., Xu, C.L., Yang, L.Z., Fang, R., Liu, W.S., 2018. Multifunctional ln-MOF luminescent probe for efficient sensing of Fe^{3+}, Ce^{3+}, and acetone. ACS Appl. Mater. Interfaces 10, 23976–23986.
Zhao, L., Kuang, X., Sun, X., Zhang, Y., Wei, Q., 2019. Synchronously achieving highly efficient hydrogen evolution and high-yield synthesis of glucaric acid by MOF nanorod arrays. J. Electrochem. Soc. 166, H534–H540.
Zhao, L., Song, X.Z., Ren, X., Fan, D.W., Wei, Q., Wu, D., 2021a. Rare self-luminous mixed-valence Eu-MOF with a self-enhanced characteristic as a near-infrared fluorescent ECL probe for nondestructive immunodetection. Anal. Chem. 93, 8613–8621.
Zhao, L., Song, X.Z., Ren, X., Wang, H., Fan, D.W., Wu, D., Wei, Q., 2021b. Ultrasensitive near-infrared electrochemiluminescence biosensor derived from Eu-MOF with antenna effect and high efficiency catalysis of specific CoS_2 hollow triple shelled nanoboxes for procalcitonin. Biosens. Bioelectron. 191, 113409.
Zhao, L., Wang, M., Song, X.Z., Liu, X.J., Ju, H.X., Ai, H.Q., Wei, Q., Wu, D., 2022. Annihilation luminescent Eu-MOF as a near-infrared electrochemiluminescence probe for trace detection of trenbolone. Chem. Eng. J. 434, 134691.